A Journal of the Gesellschaft Deutscher Chemiker

Angewandte International Edition GDCh Chemie

www.angewandte.org

Accepted Article

Title: Charge-Transport Divergence in Ultrastable Heterometal-Oxo Clusters Exerting Significant Effect on Photoreactivity

Authors: Jing-Wen Shi, Ning Li, Yan Liang, Shan Xu, Long-Zhang Dong, Dongdi Zhang, Jingyang Niu, Run-Han Li, Jiang Liu, Shun-Li Li, and Ya-Qian Lan

To be cited as: *Angew. Chem. Int. Ed.* **2025**, e202502654

Link to VoR: https://doi.org/10.1002/anie.202502654

WILEY VCH

10.1002/anie.202502654

WILEY-VCH

RESEARCH ARTICLE

Charge-Transport Divergence in Ultrastable Heterometal-Oxo Clusters Exerting Significant Effect on Photoreactivity

Jing-Wen Shi,[a][b]‡ Ning Li,[b]‡ Yan Liang,[b] Shan Xu,[b] Long-Zhang Dong,[b] Dongdi Zhang,[a]* Jingyang Niu,[a] Run-Han Li,[b]* Jiang Liu,[b] Shun-Li Li, [b]* Ya-Qian Lan [b]*

[a] J.-W. S., Prof. D. Z. and J. N.
Henan Key Laboratory of Polyoxometalate Chemistry, College of Chemistry and Chemical Engineering, Henan University, Kaifeng Henan 475004, P. R. China.

[b] J.-W. S., N. L., Y. L., S. X., L.-Z. D., R.-H. L., J. L. and Prof. Y.-Q. L.
National and Local Joint Engineering Research Center of MPTES in High Energy and Safety LIBs, Engineering Research Center of MTEES (Ministry of Education), and Key Lab. of ETESPG (GHEI), School of Chemistry, South China Normal University, Guangzhou510006, China

E-mail: ddzhang@henu.edu.cn; E-mail: lirh949@m.scnu.edu.cn; E-mail: yqlan@m.scnu.edu.cn
Homepage : http://www.yqlangroup.com/

‡ Jing-Wen Shi, and Ning Li contributed equally to this work.

Supporting information for this article is given via a link at the end of the document.

Abstract: The transfer path of photogenerated charges greatly affects the final photocatalytic performance, but this important fact has not been clearly demonstrated experimentally. Here, we construct an ultrastable crystalline catalytic system including three heterometal-oxo clusters, **Bi_8M_7-TBC4A** (M = group IVB metal-Ti/Zr/Hf), which include cubic metal-oxo cluster core with eight Bi atoms at the vertices, one M atom at the body center, and six M atoms above the cubic face centers. It is worth noted that the change of group IVB elements in **Bi_8M_7-TBC4A** can specifically modulate the LUMO-HOMO orbitals to distribute on different active metal atoms. This allows it to be an excellent model system to verify the effect of the transport paths of photogenerated charges on photoreactivity. In model reaction based on CO_2 photoreduction, **Bi_8Ti_7-TBC4A** displays superior photocatalytic CO_2-to-HCOOH conversion rate of 3,580.02 μmol g^{-1}, which is twice that of **Bi_8Zr_7-TBC4A** and 4 times that of **Bi_8Hf_7-TBC4A**. In situ characterization accompanied by density functional theory (DFT) indicate that the difference in orbital hybridization between Bi and IVB group elements largely affects the orbital distribution of frontier molecular orbital levels in **Bi_8M_7-TBC4A**, leading to the transport of photogenerated charges to metal active sites with different reactivities, and thus widely differing photocatalytic performances. This is the first model catalyst system that explores the effect of different photogenerated charge transport pathways on photoreactivity.

Introduction

Solar-driven catalytic reactions, which often exhibit the advantages of simplicity of operation and lower energy and cost, have been widely explored in catalytic chemistry to synthesize new compounds as well as to enable complex conversions.[1] In the reaction, the efficiency of photocatalysis mainly depends on the catalyst and conversion of the adsorbed substrate by efficiently utilizing the received photogenerated charge.[2] Therefore, to improve the photocatalytic reaction activity, in addition to effectively regulating the catalytic sites, ensuring that the catalyst with excellent light absorption and excellent ability in photogenerated charge separation and transport is often prioritized.[3] In this context, various strategies have been developed in the past few decades to enhance the efficiency of catalysts in utilizing sunlight.[4]

It is well-known that the efficiency of solar light utilization of catalysts depends on the processes of light absorption and utilization of photogenerated charges in separation transport.[5] At present, generous catalysts have been developed to optimize the above processes for enhancing the final photocatalytic performance.[6] However, one fact that has never received attention in these studies is that the produced photogenerated charges should be accurately transported to the most active catalyst centers/sites, which is actually extremely critical for the catalyst to effectively utilize sunlight. [7]Especially for catalyst containing different catalytic centers, if the photogenerated charges are transported to non-ideal catalytic sites, it will result in catalysts that ultimately do not achieve the desired high reactivity and solar utilization.[8]However, to date, there is still a lack of development of a suitable modeling catalyst system to demonstrate this fact.

Calixarene have the characteristics of multiple coordination sites and multiple configurations. The terminal phenolic group can bond to multiple metals, and the strong hydrophobicity of the tert-butyl group at the other end helps to protect the central metal oxygen cluster and enhance its stability.[9] Based on the above considerations, we have meticulously designed and synthesized a 4-tert-butylthiacalix[4]arene (**H4TBC4A)**-modified heterometal-oxo cluster system, **Bi_8M_7-TBC4A** (M = Ti, Zr and Hf) including a cubic metal-oxo cluster core, in which eight Bi atoms are located at the vertices of the cube, while seven Ti/Zr/Hf atoms are located above the body center and face center of the cube. Interestingly, these isostructural heterometallic clusters have the ability to regulate the direction of photogenerated charge transfer under illumination by changing the type of IVB elements (Ti, Zr or Hf) that are located above the face-center and in the body-center positions. This characteristic makes **Bi_8M_7-TBC4A** a good model catalyst system to explore the specific effect of photogenerated charge transport direction on the performance of photocatalytic reaction. Taking photocatalytic as the basic catalytic reaction, these heterometallic clusters indeed exhibited significantly different photocatalytic activity on CO_2-to-$HCOO^-$ conversion. A

10.1002/anie.202502654
WILEY-VCH

RESEARCH ARTICLE

series of in situ characterizations combined with theoretical calculation results clearly show that the difference of orbital hybridization in **Bi_8M_7-TBC4A** greatly affects the energy level distribution of the catalyst, resulting in the photogenerated electrons being mainly transferred from the TBC4A ligand to the highly active Ti(IV) site, while the photogenerated charges in **Bi_8Zr_7-TBC4A** and **Bi_8Hf_7-TBC4A** are mainly migrated from the TBC4A ligand to the metallic Bi site. Notably, the Bi(III) centers in **Bi_8M_7-TBC4A** are shown to be "electron traps" that can aggregate multi-electrons easily to greatly promote the CO_2 photoreduction activity of the catalytic active sites. These effects directly result that **Bi_8Ti_7-TBC4A** exhibits a photoreaction rate as high as 3,580.02 μmol g^{-1}, which is 2 times and 4 times that of **Bi_8Zr_7** (1,662.03 μmol g^{-1}) and **Bi_8Hf_7** (960.05 μmol g^{-1}), respectively. This work provides a model catalyst system for the first time to clearly verify the important influence of the direction of photogenerated charge transport on the photocatalytic performance.

Results and discussion

Synthesis and structure of Bi_8M_7-TBC4A. The crystal structure of **Bi_8M_7-TBC4A** is isostructural with **Pb_8Ti_7** reported in previous work,[10] which can be demonstrated by the matched powder X-ray diffraction (PXRD) patterns(Figure S1). As same as **Pb_8Ti_7**, single-crystal X-ray diffraction (SCXRD) analysis indicate that **Bi_8M_7-TBC4A** crystallizes in tetragonal *P4/nnc* space groups. The molecular structure of these clusters is composed of the inner cubic-shaped heterometal-oxo cluster core **Bi_8M_7** and six TBC4A ligands at the periphery (Figure 1). In the cubic-shaped heterometal-oxo clusters units **Bi_8M_7**, eight Bi atoms are located at the vertices of the cube, while seven Ti/Zr/Hf atoms are located at the body center and above the face center of the cube (Figure 1b). Each nine-coordinated Bi connects the S atoms of three different TBC4A ligands and is interconnected with four M atoms via several O atoms (one M at the body center and three M above the face center) to form a cubic heterometal-oxo clusters core {**Bi_8M_7-Oxo**}, which is further bonded to six peripheral TBC4A ligands by six M atoms in the perpendicular face-center direction. Each hexacoordinated M atom above the face center connects a TBC4A ligand with four phenolic O atoms in the equatorial plane and one μ_6-O and methanol molecule in the axial plane. In **Bi_8M_7-TBC4A**, the -OCH_3 group located in the axial coordination site of the M atom may be protonated and then deprotonated to expose it as an active site (Figure S2). The crystals of these three heterometal-oxo clusters appear in pale yellow under an optical microscope (Figure S3).

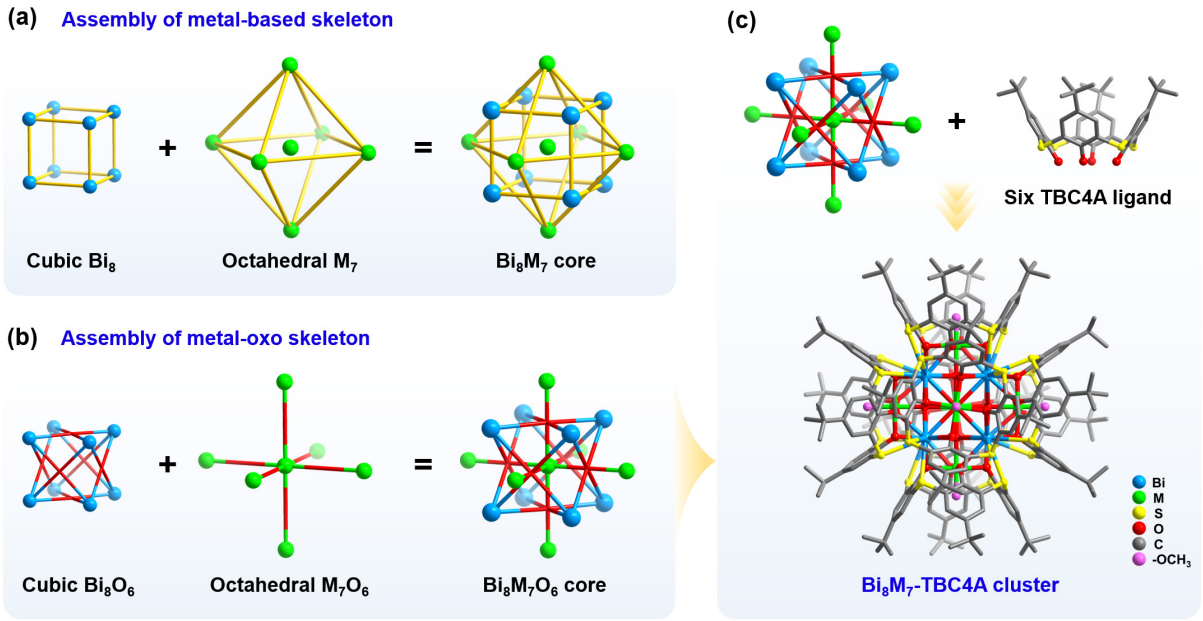

Figure 1. Crystal structure of **Bi_7M_8-TBC4A** (M = Ti, Zr and Hf; TBC4A = 4-tert-Butylthiacalix[4]arene). (a), Assembly of central metal skeleton structure of **Bi_8Ti_7-TBC4A**. (b), Assembly of central metal-oxo skeleton of **Bi_8Ti_7-TBC4A**. (c), Assembly of **Bi_7M_8-TBC4A** cluster (M = Ti, Zr or Hf). (Color codes: green Ti; light blue Bi; red O; gray C; pink -OCH_3. All H atoms have been omitted for clarity.)

The experimental powder X-ray diffraction (PXRD) patterns of the synthesized **Bi_8M_7-TBC4A** (M = Ti, Zr and Hf) match well with the simulated patterns of their single crystals, proving that all the three compounds have excellent crystallinity and high purity (Figure S1). The thermal stability of **Bi_8M_7-TBC4A** was confirmed by infrared (IR) thermogravimetry analysis (TGA) (Figure S4 and S5). In addition, **Bi_8M_7** exhibits excellent durability in air, strong acid/alkaline solutions (10 M HNO_3 or 10M KOH), which may be mainly attributed to the strong hydrophobicity of the tert-butyl group of TBC4A.[11] From the elemental mapping image, it can be seen that O, S, Bi and Ti/Zr/Hf elements are evenly distributed in the three heterometal-oxo clusters (Figure S6-S8).

The solution stabilities of these three heterometal-oxo clusters were further confirmed by Matrix-Assisted Laser Desorption/Ionization Time of Flight Mass Spectrometry (MALDI-TOF-MS) investigations. As shown in Figure S9a and Table S1, the main signal centered at m/z 6678.441 in the spectrum of **Bi_8Ti_7-TBC4A** can be attributed to a single protonated species of $\{Bi_8Ti_7(O)_{12}(TBC4A)_6[N(CH_3)_2)]_3[NH(CH_3)_2)]\}^+$ (simulated m/z as 6981.937). For **Bi_8Zr_7-TBC4A** (Figure S9b), the main signal centered at m/z 6678.441 can be attributed to $\{Bi_8Zr_7(O)_{12}(TBC_4A)_6[N(CH_3)_2)]_3[NH(CH_3)_2)]\}^+$ (simulated m/z as 6981.612). Besides, two main signals at m/z 7592.746 and 7817.171 of **Bi_8Hf_7-TBC4A** (Figure S9c) can be attributed to

10.1002/anie.202502654

$\{Bi_8Hf_7(O)_{12}(TBC4A)_6[N(CH_3)_2)]_3[NH(CH_3)_2)]\}^+$ (simulated m/z as 7592.889) and $\{Bi_8Hf_7(O)_{12}(TBC4A)_6[N(CH_3)_2)]_3[NH(CH_3)_2)_2]\}(H_2O)_{10}^+$ (simulated m/z as 7817.052), respectively. Meanwhile, we tested the metal element contents in **Bi_8M_7-TBC4A** (M = Ti, Zr and Hf) using inductively coupled plasma mass spectrometry (ICP-MS). From Table S2, it can be seen that the ratio of Bi to the corresponding Ti/Zr/Hf content in the three heterometal-oxo clusters is close to 8: 7, which is consistent with the chemical formula.

To identify the surface element composition and electronic chemical states of **Bi_8M_7-TBC4A**, X-ray photoelectron (XPS) was employed. As shown in Figure S10-S12, as for Bi of three heterometal-oxo clusters, the peaks around at 164.0 and 158.7 eV can be attributed to the $4f_{5/2}$ and $4f_{7/2}$, respectively, indicating that the oxidation state of Bi in the three heterometal-oxo clusters is 3+. For Ti, the peaks located at 465.1 and 457.6 eV are attributed to its $2p_{1/2}$ and $2p_{3/2}$, respectively, suggesting that its valence state is +4. Corresponding, the Zr 3d-binding energies (184.0 and 181.6 eV) and Hf 4f-binding energies (16.28 and18.00 eV) indicate that the two elements with the same +4 valence.

Characterizations of the optical properties of Bi_8M_7-TBC4A. The light absorption ability of **Bi_8M_7** crystals was investigated by solid-state UV/visible absorption spectroscopy, from which three heterometal-oxo clusters show obvious UV-Vis absorption bands around 200-750 nm. (Figure 2a). The band gaps (E_g), were calculated from Tauc plots to be 2.50 eV (**Bi_8Ti_7-TBC4A**), 2.58 eV (**Bi_8Zr_7-TBC4A**) and 2.36 eV (**Bi_8Hf_7-TBC4A**), respectively, indicating that all of these three clusters have semiconductor-like behaviors (Figure 2b). The HOMO levels of **Bi_8Ti_7-TBC4A**, **Bi_8Zr_7-TBC4A** and **Bi_8Hf_7-TBC4A** were determined from the UPS spectra to be 1.5, 1.59, and 1.93 V (vs. NHE), respectively, and thus corresponding to LUMO levels of -1.0, -0.99, and -0.69 V (vs. NHE), respectively (Figure 2c and Figure S13-S15).[12] The HOMO-LUMO levels can be further confirmed by Mott Schottky electrochemical measurements (Figure S16-S18). It is obvious that these three heterometal-oxo clusters have high redox potentials and potential metal activity centers, meaning that they can be used as potential catalysts for many redox reactions. The fluorescence was characterized to demonstrate the photogenerated charge transfer behavior of these heterometallic clusters. As shown in Figure 2d, the photoluminescence intensity of **Bi_8Ti_7-TBC4A** is weaker than that of the other two heterometal-oxo clusters, which means that **Bi_8Ti_7-TBC4A** has the weakest photogenerated carrier recombination ability and higher separation efficiency in photocatalysis. To investigate the light trapping behavior of the three heterometal-oxo clusters, transient photocurrent responses were carried out, and the results show that **Bi_8Ti_7-TBC4A** exhibits a higher photocurrent response compared to **Bi_8Zr_7-TBC4A** and **Bi_8Hf_7-TBC4A**, which is evidence that it possesses a more efficient photoelectron conversion ability (Figure 2e). In addition, the electrochemical impedance spectroscopy (EIS) Nyquist plots of the three heterobimetal-oxo clusters indicate that the interface charge transfer process of **Bi_8Ti_7-TBC4A** is the fastest (Figure 2f).

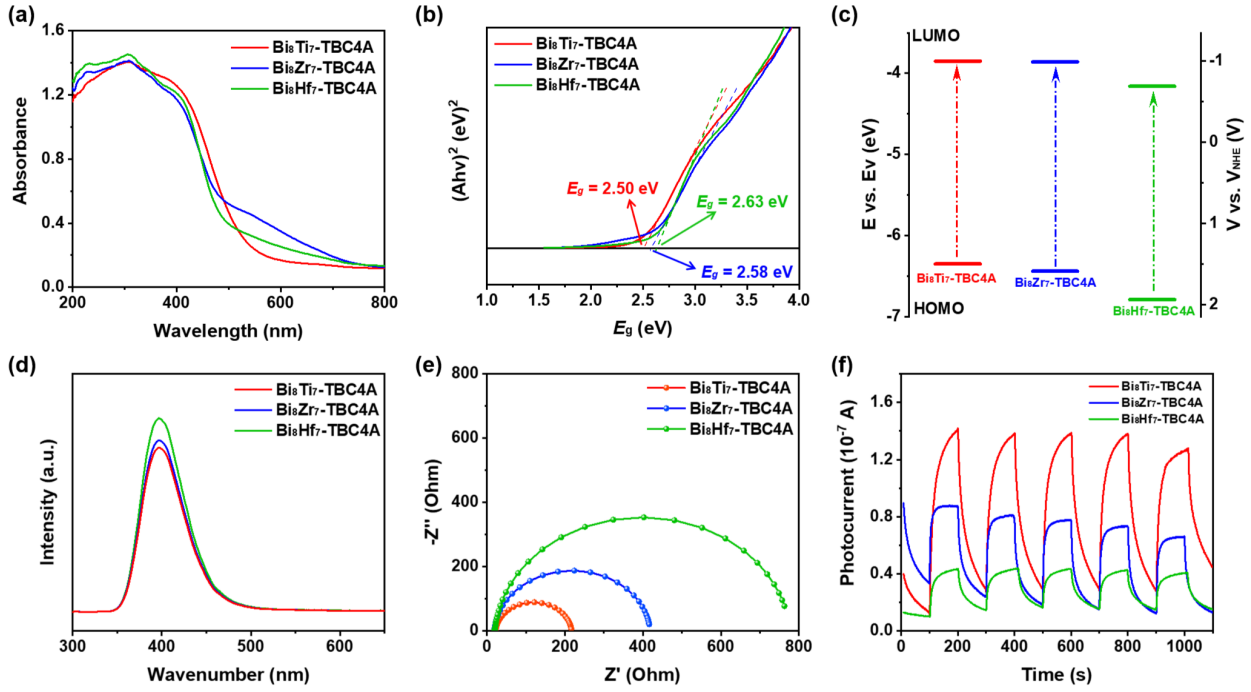

Figure 2. The optical property of **Bi_7M_8-TBC4A** (M = Ti, Zr and Hf; TBC4A = 4-tert-Butylthiacalix[4]arene). (a), UV-Vis diffuse reflectance spectra for **Bi_7M_8-TBC4A**. (b), Tauc plots of **Bi_7M_8-TBC4A**. (c), Energy band gap diagrams of **Bi_7M_8-TBC4A**. (d), Photoluminescence spectra (PL). (e), Transient photocurrent response. (f), Nyquist plots.

Photocatalytic CO_2 reduction performance. In view of the excellent light-absorbing ability and suitable energy band structure of the three heterometal-oxo clusters, we investigated the photocatalytic CO_2 reduction performance of **Bi_8Ti_7-TBC4A**, **Bi_8Zr_7-TBC4A** and **Bi_8Hf_7-TBC4A** (catalyst mass of 5 mg), respectively, under UV light using triisopropanolamine (TIPA) and H_2O as the electron sacrificial agent and reaction solution (H_2O: TIPA = 26: 4). The products were quantitatively analyzed with a test interval of three hours, the liquid phase products were quantified and characterized by ion chromatography (HPLC) (Figure S19) and ^{13}C NMR spectroscopy (Figure 3c and Figure S20), and the gas phase products were detected and quantified

by gas chromatography (GC). Under dark conditions, no product was detected; after that, the reaction system was irradiated with continuous UV light (200 - 400 nm) and $HCOO^-$ was generated immediately and increased with time, indicating that the process is a light-driven (Figure 3a). After 9 hours, the $HCOO^-$ yield of **Bi_8Ti_7-TBC4A** was as high as 17.90 ± 0.97 μmol (3,580.02 ± 194.04 μmol g^{-1}), which was 2 times and 4 times that of **Bi_8Zr_7-TBC4A** (8.31 ± 0.93 μmol, 1,662.03 ± 186.03 μmol g^{-1}) and **Bi_8Hf_7-TBC4A** (4.80 ± 0.84 μmol, 960.05 ± 168.03 μmol g^{-1}), respectively. In this work, $HCOO^-$ was the only photocatalytic liquid-phase product detected by HPLC, whereas no other CO_2 reductive products such as CO and CH_3OH that can be detected in both liquid and gas phases during the CO_2RR, indicating that the selectivity for CO_2 reduction to $HCOO^-$ of the three photocatalysts was as high as 100%. In addition, we compared the catalytic activities of **Bi_8M_7-TBC4A**, using the Turnover Number (TON). The turnover values of **Bi_8Ti_7-TBC4A**, **Bi_8Zr_7-TBC4A** and **Bi_8Hf_7-TBC4A** for the 9 h reaction were 22.3, 10.87, and 6.91, respectively, indicating that **Bi_8Ti_7-TBC4A** had higher catalytic activity than **Bi_8Zr_7-TBC4A** and **Bi_8Hf_7-TBC4A** under UV light and possessed the higher overall TON. Considering the differences in the photocatalytic CO_2 reduction performance of the three heterometal-oxo clusters, we hypothesized from the structure that the active site in **Bi_8Ti_7-TBC4A** may be a Ti atom, while the active site in **Bi_8Zr_7-TBC4A** (or **Bi_8Hf_7-TBC4A**) is a Bi atom. Therefore, the catalytic activity of **Bi_8M_7-TBC4A** (M = Ti, Zr and Hf) was compared by $TON_{actice\ site}$ of the active site. As shown in Table S3, the catalytic activity of each potential Ti site in **Bi_8Ti_7-TBC4A** is higher than that of the Bi site in **Bi_8Zr_7-TBC4A** (or **Bi_8Hf_7-TBC4A**). Therefore, the high catalytic activity of **Bi_8Ti_7-TBC4A** is mainly attributed to its potential high catalytic activity Ti site.

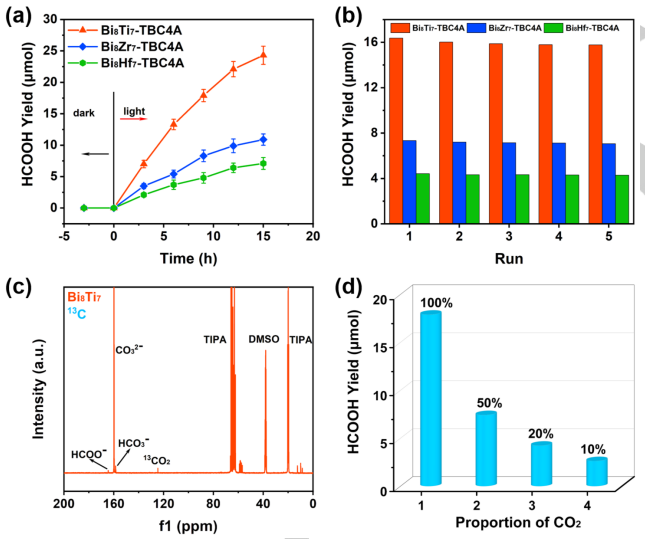

Figure 3. Photocatalytic CO_2 reduction performance of **Bi_7M_8-TBC4A** (M = Ti, Zr and Hf; TBC4A = 4-tert-Butylthiacalix[4]arene). (a), The yield of $HCOO^-$ at different time. (b), Liquid phase productions for 9 h. (c), ^{13}C NMR of possible liquid products of **Bi_8Ti_7-TBC4A** in photocatalytic $^{13}CO_2$ reduction. (d), Comparison of $HCOO^-$ produced by **Bi_8Ti_7-TBC4A** in different CO_2 concentration atmospheres.

The cyclic performance of the catalysts was then evaluated. In the cyclic test, the tested catalysts were reintroduced into a new reaction solution by centrifugation and washing in dispersion. **Bi_8M_7-TBC4A** retained more than 95% of their catalytic activity after five cycles, and the loss of catalytic activity may be due to the incomplete transfer of the catalysts during the recycling process (Figure 3b). To further demonstrate that $HCOO^-$ is obtained by conversion of CO_2, isotopic tracer experiments were performed using $^{13}CO_2$ and the origin of C in $HCOO^-$ was determined by ^{13}C NMR (Figure 3c). $HCOO^-$, CO_3^{2-} and HCO_3^- can be clearly seen from the ^{13}C NMR spectra, which is consistent with other previous work. In addition, when photocatalytic tests were performed using $^{12}CO_2$, the peaks disappeared at other positions except for the characteristic peaks of DMSO and TIPA (Figure S20). This experimental result suggests that all the $HCOO^-$ produced is obtained by the reductive conversion of CO_2. Therefore **Bi_8Ti_7-TBC4A** is able to reduce CO_2 to $HCOO^-$ under UV light. In addition, photocatalytic CO_2 reduction experiments were carried out on **Bi_8Ti_7-TBC4A** under low concentration CO_2, which is of practical significance compared with the photocatalytic reduction under pure CO_2 atmosphere. As can be seen from the Figure 3d, the reduction rate of CO_2 by **Bi_8Ti_7-TBC4A** can still reach 58.44 μmol μmol g^{-1} h^{-1} at 10% CO_2 content (CO_2: Ar = 1: 9). These three heterometal-oxo clusters catalysts did not dissolve and exhibited good crystallinity after photocatalytic CO_2RR, thus proving the nature of their heterogeneous catalysts. To further demonstrate stability, the solid catalysts were isolated after the photocatalytic CO_2RR reaction and tested by solid-state infrared (FTIR) (Figure S21-S23) and PXRD (Figure S24). The results showed that the PXRD patterns and FTIR patterns of these three heterometal-oxo clusters catalysts before and after the photocatalytic CO_2RR were almost unchanged, proving their high crystallinity and stability. The XPS of samples before and after the reaction were also used to demonstrate the stability of **Bi_8M_7-TBC4A**. As show in Figure S25-R27, the XPS spectra of the samples before and after the test are basically consistent, proving that the performance of the three heterometal-oxo cluster photocatalysts is stable during the photocatalytic test.

Studies on the Photocatalytic Reaction Mechanism. In-situ XPS measurements were used to confirm the electron transfer process in the photocatalytic reaction through the change in the binding energy of the elements. As shown in the Figure 4a and 4b, when **Bi_8Ti_7-TBC4A** was illuminated under Ar dark conditions, the Ti *2p* binding energy decreases from 464.73 and 457.60 eV to 464.12 and 457.34 eV, respectively, and the Bi *4f* binding energy decreases from 164.00 and 158.71 eV to 163.68 and 158.49 eV, respectively. This suggests that under illumination, the photogenerated electrons of **Bi_8Ti_7-TBC4A** can be transferred to the metal-oxo cluster center. After introducing CO_2 into the system, the binding energy of Bi *4f* increased and returned to the ground state, while the binding energy of Ti *2p* increased by 0.21 eV. Combined with the structural analysis of **Bi_8Ti_7-TBC4A**, it can be seen that the direction of the transfer of photogenerated electrons during the photocatalytic process is transferred from Bi atoms to Ti atoms and finally to CO_2, and this result suggests that the center of the cubic bismuth-oxo clusters can act as an "electron trap" for accommodating photogenerated charges (Figure 4d and 4e) and quickly transferred to the catalytically active center during the photocatalytic process to promote the rapid reduction of CO_2.[6a, 13] Based on the above results, the photocatalytic CO_2RR of **Bi_8Ti_7-TBC4A** can be reasonably explained as follows: under light, the calixarene generate photogenerated charges and then transfer them to the central metal-oxo cluster centers, which act as electron traps capable of accommodating the photogenerated charges and the reduction of

10.1002/anie.202502654

Ti^{4+} to Ti^{3+} species, while TIPA acts as a hole (h^+) scavenger. Photogenerated electrons are then transferred from the central bismuth-oxo cluster electron trap to the catalytic center Ti atoms via the oxygen bridge between Bi-Ti and ultimately to CO_2 adsorbed on the active metal Ti sites. When the fourth subgroup metals are Zr and Hf, the photogenerated charge is then transferred from the calixarene to the bismuth-oxo cluster centers during photoexcitation and from the bismuth-oxo cluster centers back to the CO_2 reduction centers during CO_2 reduction (Figure 4d).To investigate the photogenerated electron transfer pathway of **Bi_8Ti_7-TBC4A** in photocatalytic CO_2 reduction, the photocatalytic CO_2RR mechanism was investigated using in situ electron paramagnetic resonance (EPR) spectroscopy (Figure 4c). The results showed that in the reaction system containing **Bi_8Ti_7-TBC4A** and TIPA as well as CO_2 atmosphere, no ESR signal appeared under dark conditions. When the reaction system was irradiated with UV light for 30 min, a significant signal change could be observed in the ESR spectra. The signal at g = 1.944 could be attributed to the characteristic signal of Ti^{3+} ions, which implies that Ti^{4+} at the center of the metal-oxo clusters in **Bi_8Ti_7-TBC4A** accepts photogenerated electrons produced by calixarene via ligand-to-metal charge transfer (LMCT) upon photoexcitation.[14] The strong signal at g = 2.002, on the other hand, was attributed to the oxygen vacancies formed by the unsaturated coordination metal atoms in the heterometal-oxo clusters, which implies that **Bi_8Ti_7-TBC4A** has active sites that can adsorb and reduce CO_2.[15]

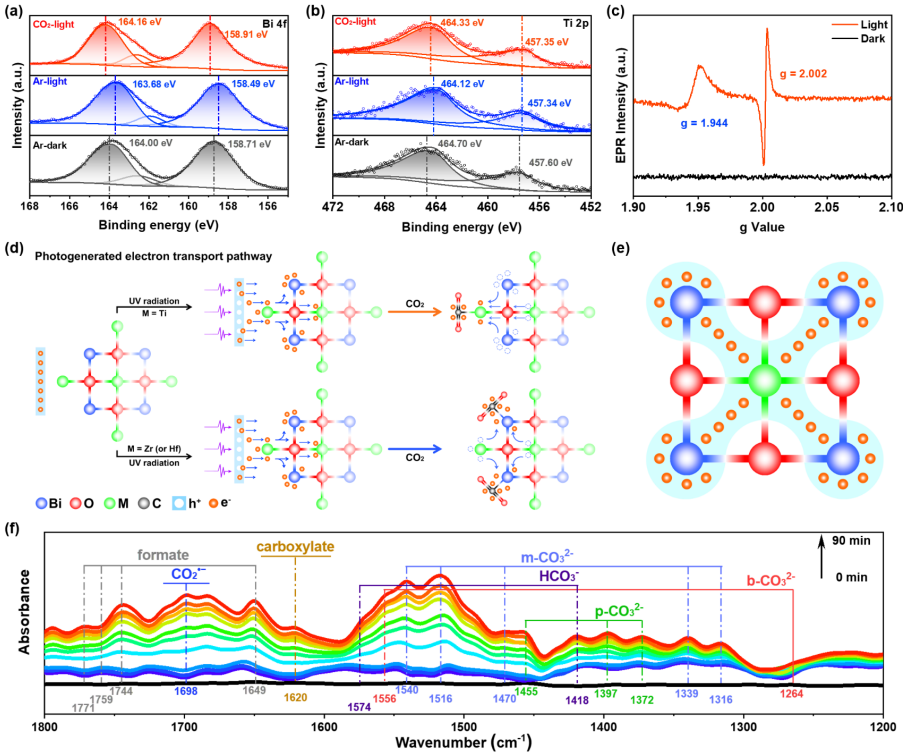

Figure 4. High-resolution X-ray photoelectron spectroscopy (XPS) of (a) Bi *4f* and (b) Ti *2p*. (c) ESR spectra of **Bi_8Ti_7-TBC4A** clusters before and after light irradiation. (d) Schematic cross-section of the electron transfer pathway of **Bi_8M_7-TBC4A**. (e) Schematic diagram of the cross section of the "electron trap" formed by the central metal-oxo cluster. (f) In situ FTIR spectra on **Bi_8Ti_7-TBC4A** under UV light irradiation and a CO_2 atmosphere.

To demonstrate the CO_2-to-HCOOH conversion process of **Bi_8M_7-TBC4A**, in situ diffuse reflectance infrared fourier-transform spectroscopy (DRIFTS) was used to detect CO_2 radicals and intermediates in the photocatalytic CO_2RR process using **Bi_8Ti_7-TBC4A** as a representative catalyst. As shown in the Figure 4f, no significant change in the vibrational peak were detected under dark conditions. As the illumination time increases from 0 to 90 mins, the formation of new vibrational peaks could be clearly detected with a gradual increase in intensity. The absorption peaks at 1316, 1339, 1470, 1516, and 1540 cm^{-1} could be attributed to the monodentate carbonate (m-CO_3^{2-}), while the absorption peaks at absorption peaks at 1264 and 1556 cm^{-1} could be attributed to bidentate carbonates (b-CO_3^{2-}).[16] In addition, the absorption peaks at 1372, 1397, and 1455 cm^{-1} can be attributed to polydentate carbonate (p-CO_3^{2-}), and the peaks at 1418 and 1574 cm^{-1} were attributed to bicarbonate (HCO_3^-).[14] The significant increase in the intensity of these carbonate peaks indicates that **Bi_8Ti_7-TBC4A** can adsorb CO_2 and form interactions with it. The appearance of peaks at 1649, 1744, 1759, and 1771 cm^{-1} may be a result of formate, while the peak at 1620 is most likely attributed to carboxylate.[17] A significant enhancement of the absorption peak can be observed at 1698 cm^{-1}, which is attributed to $CO_2^{\bullet-}$ radical, which is an important single-electron reduction intermediate in the photocatalytic reduction to $HCOO^-$.[18]To deeply investigate the catalytic differences among the three heterometal-oxo clusters, DFT calculations related to CO_2 adsorption and activation were carried out for the three heterometal-oxo clusters to confirm the active sites. The calculated frontier molecular orbital distributions show that the highest occupied molecular orbital (HOMO) of the three heterometal-oxo clusters are mainly concentrated on the calixarene ligands (Figure 5a). Diversely, the distribution of the lowest unoccupied molecular orbital (LUMO) orbitals of the **Bi_8Ti_7-TBC4A** structure is mainly concentrated on the Ti atoms, while the LUMO orbitals of the **Bi_8Zr_7-TBC4A** and **Bi_8Hf_7-TBC4A** structures have a similar distribution and are distributed only on

10.1002/anie.202502654

Bi. This indicates that the excited hole positions are almost located in **TBC4A** parts, while excited electron positions of the three clusters are different. Specifically, after excitation, the electrons of the **Bi_8Ti_7-TBC4A** are transferred to the Ti atoms, so the site of the reduction reaction is also more likely located on Ti atoms. For **Bi_8Zr_7-TBC4A** and **Bi_8Hf_7-TBC4A**, the reduction catalytic site is located in Bi atoms, which is why the catalytic performance is significantly different. The spin density distribution calculation also verifies that the electrons of reduced **Bi_8Ti_7-TBC4A** are distributed on Ti atoms, and **Bi_8Zr_7-TBC4A** and **Bi_8Hf_7-TBC4A** are distributed on Bi atoms (Figure S28).

Furthermore, the total density of states (TDOS) and partial density of states (PDOS) of the three systems **Bi_8M_7-TBC4A** were also calculated and plotted by dividing the three systems into four moieties, namely, Bi atoms, Ti (Zr/Hf) atoms, O atoms, and TBC4A parts, respectively (Figure 5b-5d). Through the PDOS diagram, it can be analyzed that the density of occupied states near the Fermi level of the three systems is mainly contributed by TBC4A ligands, and the corresponding unoccupied states are co-contributed by Ti (Zr or Hf), Bi atoms and TBC4A. It is noteworthy that in the unoccupied state parts, the Ti metal atoms of **Bi_8Ti_7-TBC4A** are distributed in the lower energy level, and a special and isolated unoccupied state appears near the Fermi level. That makes the energy gap of **Bi_8Ti_7-TBC4A** reduced significantly and the LMCT transition easier to be realized. In contrast, the energy gap of **Bi_8Zr_7-TBC4A** and **Bi_8Hf_7-TBC4A** is higher, and the orbital overlap occurs in unoccupied state of Bi moieties and **TBC4A**. Therefore, after excitation, electrons are more easily transferred between the Bi moieties and **TBC4A**. This result is consistent with the orbital energy level diagram we obtained above, and also reflects that in the catalytic process, the catalytic site of **Bi_8Ti_7-TBC4A** mainly provides by Ti sites.

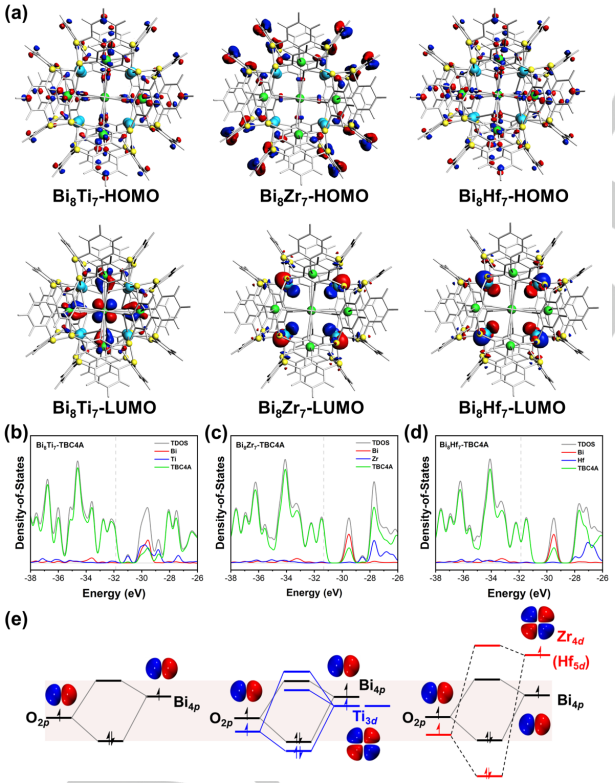

Figure 5. (a), LOMO and HOMO orbital distribution diagram of **Bi_7M_8-TBC4A**. (b-d), Total and projected DOS of **Bi_7M_8-TBC4A**. (e), Hybrid orbital distribution diagram of **Bi-O**, **BiTi-O** and **BiZr-O** (or **BiHf-O**).

As illustrated in Figure 5e, the differences in the LUMO and HOMO distributions of the three heterometal-oxo clusters can be understood better. In the absence of Ti/Zr/Hf metal doping, the *4p* atomic orbital of Bi are linearly combined with the *2p* atomic orbital of O to form a pair of bonding-antibonding orbitals. When Ti metal atoms are doped, the *3d* orbital level of titanium is similar to and slightly lower than the *4p* orbital level of bismuth. Therefore, the bonding and antibonding orbitals of Ti-O are arranged in a position similar to the orbital energy levels of the Bi-O bond. In addition, the lower *3d* empty orbitals of titanium are converted into the LUMO of **Bi_8Ti_7-TBC4A** clusters, which regulates the distribution of frontier molecular orbitals of clusters to affect the catalytic sites and reactivity. However, for the **Bi_8Zr_7-TBC4A** and **Bi_8Hf_7-TBC4A** cases, the corresponding atomic orbitals of zirconium and hafnium are much higher than the atomic orbitals of Bi, so the resulting bonding and antibonding pairs cannot be distributed in the frontier orbital positions of the molecule. Therefore, the unoccupied orbitals are more distributed on Bi and TBC4A sites.

Combined with in situ XPS results, for **Bi_8Ti_7-TBC4A**, it can be seen that the empty orbitals distributed in bismuth and titanium have accepted electrons through LMCT process after light excitation. When CO_2 is introduced into the system, the exposed Ti sites will firstly transfer electrons to CO_2 as reduction sites. Due to the orbital overlap effect of bismuth and titanium, the electrons located in bismuth are transferred to the *3d* orbital of titanium attributed to LUMO through the BI-O-Ti path, thus completing the subsequent CO_2 reduction process. For **Bi_8Zr_7-TBC4A** and **Bi_8Hf_7-TBC4A**, the photogenerated electrons are directly transferred to bismuth-oxo clusters via by calixarene. These reasons led to the much larger photocatalytic CO_2 reduction activity of **Bi_8Ti_7-TBC4A** than that of **Bi_8Zr_7-TBC4A** and **Bi_8Hf_7-TBC4A**. To verify this hypothesis, we specifically studied the adsorption energy of CO_2 at different sites on **Bi_8M_7-TBC4A**. Figure S29-31 shows the optimized model for the adsorption of CO_2 on the surface of different sites. The adsorption energies of CO_2 at the Ti, S and Bi sites of **Bi_8Ti_7-TBC4A** are -16.59, -6.94 and -7.35 kcal mol^{-1}, respectively. Obviously, the Ti site shows lower adsorption energy than S and Bi, indicating that the Ti site can effectively enhance the adsorption of CO_2. However, for **Bi_8Zr_7-TBC4A** and **Bi_8Hf_7-TBC4A**, the adsorption energy of the Bi site is the lowest, which is -7.90 and -7.11 kcal mol^{-1}, respectively, which means that when the IVB group atoms are Zr and Hf, CO_2 is more easily adsorbed on the Bi site. The energy changes of **Bi_8Ti_7-TBC4A**, **Bi_8Zf_7-TBC4A**, and **Bi_8Hf_7-TBC4A** for reduction of CO_2 to HCOOH also show that lower barrier has been required with **Bi_8Ti_7-TBC4A** as a catalyst, further proving the higher catalytic performance of **Bi_8Ti_7-TBC4A** (Figrue S32 and S33).

Conclusion

In conclusion, we have elaborately constructed a series of isostructural crystalline model catalysts, consisting of a cubic metal-oxygen cluster center and six M atoms coordinated by calixarene located above the face center of the cube, whose frontier molecular orbital distributions can be effectively tuned by changing the IVB group metal elements above the face centers of

the cubes. This causes the photogenerated charges to transfer along the Ti-O-Bi-O-Ti-CO_2 and Zr/Hf-O-Bi-O-Bi-CO_2 directions on **Bi_8Ti_7-TBC4A** and **Bi_8Zr/Hf_7-TBC_4A**, respectively, and reach metal active sites with different reactivity (Ti and Bi), ultimately showing large differences in CO_2 photoreduction reactivity. This is the first time to clearly demonstrate the important effect of different photogenerated charge transport paths on the photoreactivity by using crystalline model catalysts.

Acknowledgements

This work was financially supported by the National Key R&D Program of China (2024YFA1510700 and 2023YFA1507204). The National Natural Science Foundation of China (Grants 22271104, 22071045, 22201046, 22301084 22371080 and 22301085). China Postdoctoral Science Foundation (No. 2023M741232). Natural Science Foundation of Guangdong Province (2024A1515011250).

Conflict of Interest

The authors declare no conflict of interest.

Keywords: Heterometal-oxo clusters • photocatalysis • photoelectron transport • CO_2 reduction

References

[1] a) D. M. Schultz, T. P. Yoon, *Science* **2014**, *343*, 1239176; b) F. Parrino, V. Loddo, V. Augugliaro, G. Camera-Roda, G. Palmisano, L. Palmisano, S. Yurdakal, *Catal. Rev.* **2019**, *61*, 163-213; c) Y. Guo, T. Li, D. Li, J. Cheng, *Renew.Sustain. Energ. Rev.* **2024**, *189*, 114053; d) S. Fang, M. Rahaman, J. Bharti, E. Reisner, M. Robert, G. A. Ozin, Y. H. Hu, *Nat. Rev. Method. Prim.* **2023**, *3*, 61.

[2] a) J. Kou, C. Lu, J. Wang, Y. Chen, Z. Xu, R. S. Varma, *Chem. Rev.* **2017**, *117*, 1445-1514; b) K. Song, H. Liu, B. Chen, C. Gong, J. Ding, T. Wang, E. Liu, L. Ma, N. Zhao, F. He, *Chem. Rev.* **2024**; c) T. Hang, L. Wu, W. Liu, L. Yang, T. Zhang, *Adv. Energ. Sust. Res.* **2024**, *5*, 2400069.

[3] a) F. Li, L. Cheng, J. Fan, Q. Xiang, *J. Mater. Chem. A* **2021**, *9*, 23765-23782; b) J. Zhang, J. Jiang, Y. Lei, H. Liu, X. Tang, H. Yi, X. Huang, S. Zhao, Y. Zhou, F. Gao, *Sep. Purif. Technol.* **2024**, *328*, 125056; c) F. Chen, T. Ma, T. Zhang, Y. Zhang, H. Huang, *Adv. Mater.* **2021**, *33*, 2005256.

[4] B. Zhang, L. Sun, *Chem. Soc. Rev.* **2019**, *48*, 2216-2264.

[5] a) M.-Q. Yang, M. Gao, M. Hong, G. W. Ho, *Adv. Mater.* **2018**, *30*, 1802894; b) C. Feng, Z.-P. Wu, K.-W. Huang, J. Ye, H. Zhang, *Adv. Mater.* **2022**, *34*, 2200180.

[6] a) J. Zhou, J. Li, L. Kan, L. Zhang, Q. Huang, Y. Yan, Y. Chen, J. Liu, S.-L. Li, Y.-Q. Lan, *Nat. Commun.* **2022**, *13*, 4681; b) K. Sekizawa, K. Maeda, K. Domen, K. Koike, O. Ishitani, *J. Am. Chem. Soc.* **2013**, *135*, 4596-4599; c) M. Lu, S.-B. Zhang, R.-H. Li, L.-Z. Dong, M.-Y. Yang, P. Huang, Y.-F. Liu, Z.-H. Li, H. Zhang, M. Zhang, S.-L. Li, Y.-Q. Lan, *J. Am. Chem. Soc.* **2024**, *146*, 25832-25840; d) Y. Tao, J. Guan, J. Zhang, S. Hu, R. Ma, H. Zheng, J. Gong, Z. Zhuang, S. Liu, H. Ou, D. Wang, Y. Xiong, *Angew. Chem. Int. Ed.* **2024**, *63*, e202400625; e) K. Yuan, K. Tao, T. Song, Y. Zhang, T. Zhang, F. Wang, S. Duan, Z. Chen, L. Li, X. Zhang, D. Zhong, Z. Tang, T.-B. Lu, W. Hu, *J. Am. Chem. Soc.* **2024**, *146*, 6893-6904; f) J.-M. Lin, Z.-B. Mei, C. Guo, J.-R. Li, Y. Kuang, J.-W. Shi, J.-J. Liu, X. Li, S.-L. Li, J. Liu, Y.-Q. Lan, *J. Am. Chem. Soc.* **2024**, *146*, 22797-22806.

[7] a) H. Ou, S. Ning, P. Zhu, S. Chen, A. Han, Q. Kang, Z. Hu, J. Ye, D. Wang, Y. Li, *Angew. Chem. Int. Ed.* **2022**, *61*, e202206579; b) J.-N. Lu, J.-J. Liu, L.-Z. Dong, J.-M. Lin, F. Yu, J. Liu, Y.-Q. Lan, *Angew. Chem. Int. Ed.* **2023**, *62*, e202308505; c) H. Yu, J. Huang, L. Jiang, X. Yuan, K. Yi, W. Zhang, J. Zhang, H. Chen, *Chem. Eng. J.* **2021**, *408*, 127334.

[8] a) T. Zhang, W. Li, K. Huang, H. Guo, Z. Li, Y. Fang, R. M. Yadav, V. Shanov, P. M. Ajayan, L. Wang, C. Lian, J. Wu, *Nat. Commun.* **2021**, *12*, 5265; b) L. Li, R. Zhang, P. Hou, Y. Lin, D. Wang, T. Xie, *ACS Catal.* **2023**, *13*, 10824-10834; c) M. Zhou, Z. Wang, A. Mei, Z. Yang, W. Chen, S. Ou, S. Wang, K. Chen, P. Reiss, K. Qi, J. Ma, Y. Liu, *Nat. Commun.* **2023**, *14*, 2473; d) M. Li, S. Wu, D. Liu, Z. Ye, L. Wang, M. Kan, Z. Ye, M. Khan, J. Zhang, *J. Am. Chem. Soc.* **2024**, *146*, 15538-15548; e) S. Zhang, B. Johannessen, B. Xia, X. Gao, K. Davey, J. Ran, S.-Z. Qiao, *J. Am. Chem. Soc.* **2024**, *146*, 32003-32012.

[9] a) X.-Y. Chen, Q.-Y. Liu, W.-D. Yu, J. Yan, C. Liu, *Chem. Commun.* **2024**, *60*, 11890-11898; b) I. V. Khariushin, V. Bulach, S. E. Solovieva, I. S. Antipin, A. S. Ovsyannikov, S. Ferlay, *Coord. Chem. Rev.* **2024**, *513*, 215846; c) M. Coletta, E. K. Brechin, S. J. Dalgarno, *Calixarenes and Beyond* **2016**, pp. 671-689; d) B. Hou, H. Zheng, K. Zhang, Q. Wu, C. Qin, C. Sun, Q. Pan, Z. Kang, X. Wang, Z. Su, *Chem. Sci.* **2023**, *14*, 8962-8969.

[10] S. Zhou, C. Li, H. Fu, J. Cao, J. Zhang, L. Zhang, *Chem. Eur. J.* **2020**, *26*, 6894-6898.

[11] a) N. Li, J.-J. Liu, J.-W. Sun, B.-X. Dong, L.-Z. Dong, S.-J. Yao, Z. Xin, S.-L. Li, Y.-Q. Lan, *Green Chem.* **2020**, *22*, 5325-5332; b) Z.-J. Guan, F. Hu, S.-F. Yuan, Z.-A. Nan, Y.-M. Lin, Q.-M. Wang, *Chem. Sci.* **2019**, *10*, 3360-3365; c) S.-N. Sun, Q. Niu, J.-M. Lin, L.-L. He, J.-W. Shi, Q. Huang, J. Liu, Y.-Q. Lan, *Sci. Bull.* **2024**, *69*, 492-501; d) J.-W. Shi, S.-N. Sun, J. Liu, Q. Niu, L.-Z. Dong, Q. Huang, J.-J. Liu, R. Wang, Z. Xin, D. Zhang, J. Niu, Y.-Q. Lan, *ACS Catal.* **2022**, *12*, 14436-14444.

[12] J. Liu, Y. Liu, N. Liu, Y. Han, X. Zhang, H. Huang, Y. Lifshitz, S.-T. Lee, J. Zhong, Z. Kang, *Science* **2015**, *347*, 970-974.

[13] a) C. Bie, B. Zhu, F. Xu, L. Zhang, J. Yu, *Adv. Mater.* **2019**, *31*, 1902868; b) F. Xu, K. Meng, B. Cheng, S. Wang, J. Xu, J. Yu, *Nat. Commun.* **2020**, *11*, 4613; c) L. Wang, B. Cheng, L. Zhang, J. Yu, *Small* **2021**, *17*, 2103447.

[14] N. Li, J.-M. Lin, R.-H. Li, J.-W. Shi, L.-Z. Dong, J. Liu, J. He, Y.-Q. Lan, *J. Am. Chem. Soc.* **2023**, *145*, 16098-16108.

[15] S. Yang, X. Guo, X. Li, T. Wu, L. Zou, Z. He, Q. Xu, J. Zheng, L. Chen, Q. Wang, Z. J. Xu, *Angew. Chem. Int. Ed.* **2024**, *63*, e202317957.

[16] M. Kou, W. Liu, Y. Wang, J. Huang, Y. Chen, Y. Zhou, Y. Chen, M. Ma, K. Lei, H. Xie, P. K. Wong, L. Ye, *Appl. Catal. B* **2021**, *291*, 120146.

[17] Y. Xi, X. Zhang, Y. Shen, W. Dong, Z. Fan, K. Wang, S. Zhong, S. Bai, *Appl. Catal. B* **2021**, *297*, 120411.

[18] X.-F. Qiu, H.-L. Zhu, J.-R. Huang, P.-Q. Liao, X.-M. Chen, *J. Am. Chem. Soc.* **2021**, *143*, 7242-7246.

10.1002/anie.202502654

WILEY-VCH

RESEARCH ARTICLE

Entry for the Table of Contents

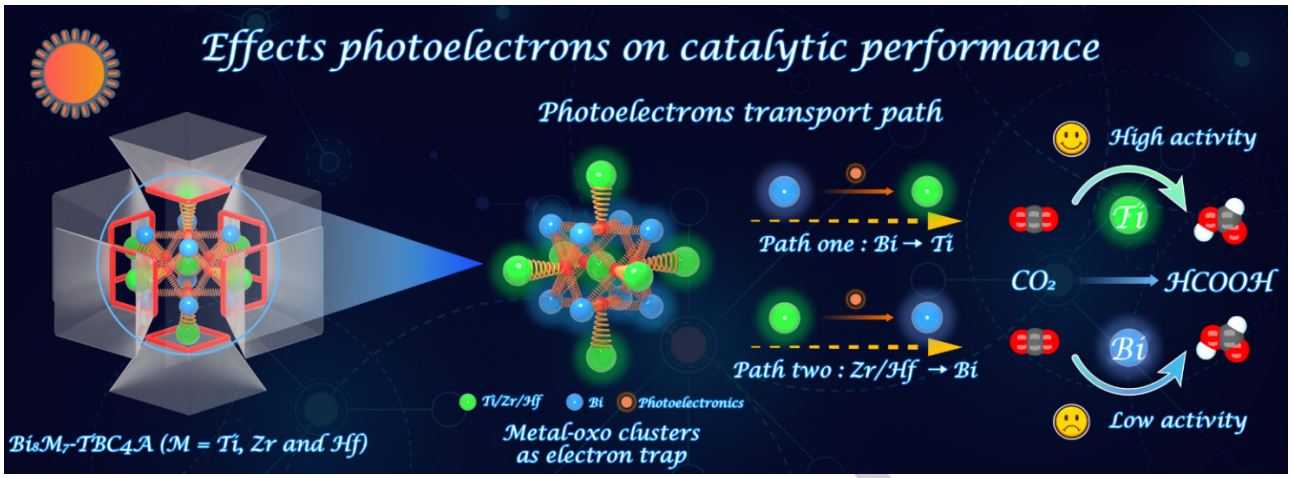

The difference in orbital hybridization between heterometallic elements in heterometal-oxo clusters **Bi_8M_7-TBC4A** (M = Ti, Zr and Hf) has a significant effect on the distribution of frontier molecular orbital energy levels, resulting in the transmission of photogenerated electrons to different active sites, thus leading to different catalytic activities.